Zitierweise: *Angew. Chem. Int. Ed.* **2024**, *63*, e202407380
doi.org/10.1002/anie.202407380

Batteries **Hot Paper**

Single-Anion Conductive Solid-State Electrolytes with Hierarchical Ionic Highways for Flexible Zinc-Air Battery

Mi Xu, Rui Cao, Boying Hao, Dongdong Wang, Dan Luo, Haozhen Dou, and Zhongwei Chen**

Abstract: Flexible zinc-air batteries are leading power sources for next-generation smart wearable electronics. However, flexible zinc-air batteries suffer from the highly-corrosive safety risk and limited lifespan due to the absence of reliable solid-state electrolytes (SSEs). Herein, a single-anion conductive SSE with high-safety is constructed by incorporating a highly amorphous dual-cation ionomer into a robust hybrid matrix of functional carbon nanotubes and polyacrylamide polymer. The as-fabricated SSE obtains dual-penetrating ionomer-polymer networks and hierarchical ionic highways, which contribute to mechanical robustness with 1200 % stretchability, decent water uptake and retention, and superhigh ion conductivity of 245 $mS \cdot cm^{-1}$ and good Zn anode reversibility. Remarkably, the flexible solid-state zinc-air batteries delivers a high specific capacity of 764 $mAh \cdot g^{-1}$ and peak power density of 152 $mW \cdot cm^{-2}$ as well as sustains excellent cycling stability for 1050 cycles (350 hours). This work offers a new paradigm of OH^- conductors and broadens the definition and scope of OH^- conductors.

Introduction

Zinc-air batteries adopt the naturally abundant zinc anode and porous air cathode with infinite oxygen supplied from air,[1] and solid-state rechargeable zinc-air batteries offer inherent safety, flexibility, and cost-effectiveness,[2] which are the leading power sources for the fast-growing portable and wearable electronics.[3] However, the popularization of flexible zinc-air batteries is severely hindered by the limited cycling life.[4] The main challenge is the absence of reliable solid-state electrolytes (SSEs).[5] The widely used SSEs are the gel polymer electrolytes (GPEs), which are composed of KOH solution and inert polymer matrixes such as polyvinyl alcohol (PVA) and polyacrylamide (PAM).[6] Although owning good water uptake and retention as well as high ion conductivity,[7] high corrosion of KOH solution and the potential structure instability for GPEs under highly corrosive electrochemical environment cause the severe safety risks and battery failure.[8] Anion-exchange membranes (AEMs) or their analogues, as another type of SSEs, are a rigid polymer backbone functionalized with positive-charged groups to conduct hydroxide ion (OH^-) counter anion,[9] which have the attributes of high safety and also promote Zn anode reversibility by suppressing dendrite growth and corrosion reactions. However, the low ion conductivity and poor water uptake of AEMs lead to the fast degradation of battery performance within several hours (8–10 hours).[10] Therefore, innovative design strategy for ideal SSEs with the advantages of both GPEs and AEMs is highly desired and truly matter in practical application of flexible zinc-air batteries.

In nature, plant roots and blood circulatory system allows for highly efficient mass transfer due to their hierarchical transport highways.[11] For example, plant roots composed of primary lateral roots, secondary lateral roots and taproot can ingeniously realize the fast uptake and transportation of water, inorganic salts and some trace elements to ensure the plant growth.[12] Therefore, the hierarchical structure and function of fast mass transfer of plant root system and blood circulatory system provide archetypes and grant germane inspirations for constructing hierarchical transport highways to develop ideal SSEs.[13] Single OH^- conductive ionomer can conduct OH^- like AEMs and have high ion transference number to avoid a concentration gradient on the Zn anode, which affords the high-safety and promotes Zn anode reversibility.[14] The molecular structure of ionomer is tailorable with high cation density and chain flexibility to enhance OH^- conductivity.[15] More importantly, ionomer offers an attractive option for constructing three-dimensional (3D) ionic highway.[16] Hydrophilic polymer can guarantee good water uptake and retention like GPEs, and is promising candidate to form a dual-network structure with ionomer.[17] The dual-penetrating networks that combines a hydrophilic polymer and a single OH^- conductive ionomer not only affords the mechanical robustness but also contribute to formation of abundant interfacial ionic highway between hydrophilic polymer and ionomer. Moreover, one-dimensional (1D) nanomaterials such as carbon nanotubes are widely utilized to construct the 1D ionic highway via surface modification and can also perform as the reinforcing agent for SSEs.[18]

[*] M. Xu, R. Cao, B. Hao, D. Wang, D. Luo, H. Dou, Prof. Z. Chen
State Key Laboratory of Catalysis, Power Battery & System Research Center, Dalian Institute of Chemical Physics, Chinese Academy of Sciences, Dalian, 110623, China
E-mail: zwchen@dicp.ac.cn
haozhen@dicp.ac.cn
M. Xu, Prof. Z. Chen
Department of Chemical Engineering, University of Waterloo, Waterloo, ON N2L 3G1, Canada

Therefore, hybridization of functional CNT within SSEs can further enhance the ion conductivity and mechanical property.

Herein, inspired by plant roots and blood circulatory system (Figure 1a), we construct single-anion conductive SSEs with hierarchical ionic highways (Figure 1b) for flexible zinc-air battery. The SSEs are constructed by in situ polymerization of single OH^--conductive ionomer (PVImBO) within the hybrid matrix of functional carbon nanotubes (FCNTs) and PAM hydrophilic polymer (FCNT/PAM) to form dynamical dual-penetrating networks (Figure 1c–d). As for the molecular design of ionomer network, a novel hydrophilic alkoxy linker connected dual-cation monomer (VImBO) is designed for the first time as building block, where the imidazolium dual-cations with good chemical stability favor for high ion density and the hydrophilic alkoxy links promote the chain flexibility and self-assembly to build the connected highways. Regarding to the polymer network, PAM is selected due to its robust mechanical property and good water retention capacity, and the impregnation of OH^--conductive FCNTs with PAM further enhances ion conductivity and mechanical robustness. The SSEs ingeniously integrate the advantages of traditional GPEs and AEMs but overcome their shortcomings. The SSEs conduct OH^- like AEMs and avoid the highly corrosive KOH solution, which can be interpreted as single-ion conductive GPEs or gel-state AEMs. More importantly, the SSEs foster new functionalities, where the hierarchical ionic highways consisting of 3D highway from penetrating network of PVImBO, 1D highway from FCNT and interfacial highway between PVImBO and PAM (Figure S1) are generated for superfast OH^- conduction. As expected, single-anion conductive SSEs deliver the superhigh ion conductivity of 245 $mS \cdot cm^{-1}$, superior water-retaining capability, good structure stability, and mechanical robustness with stretchability of 1000 % and also suppress

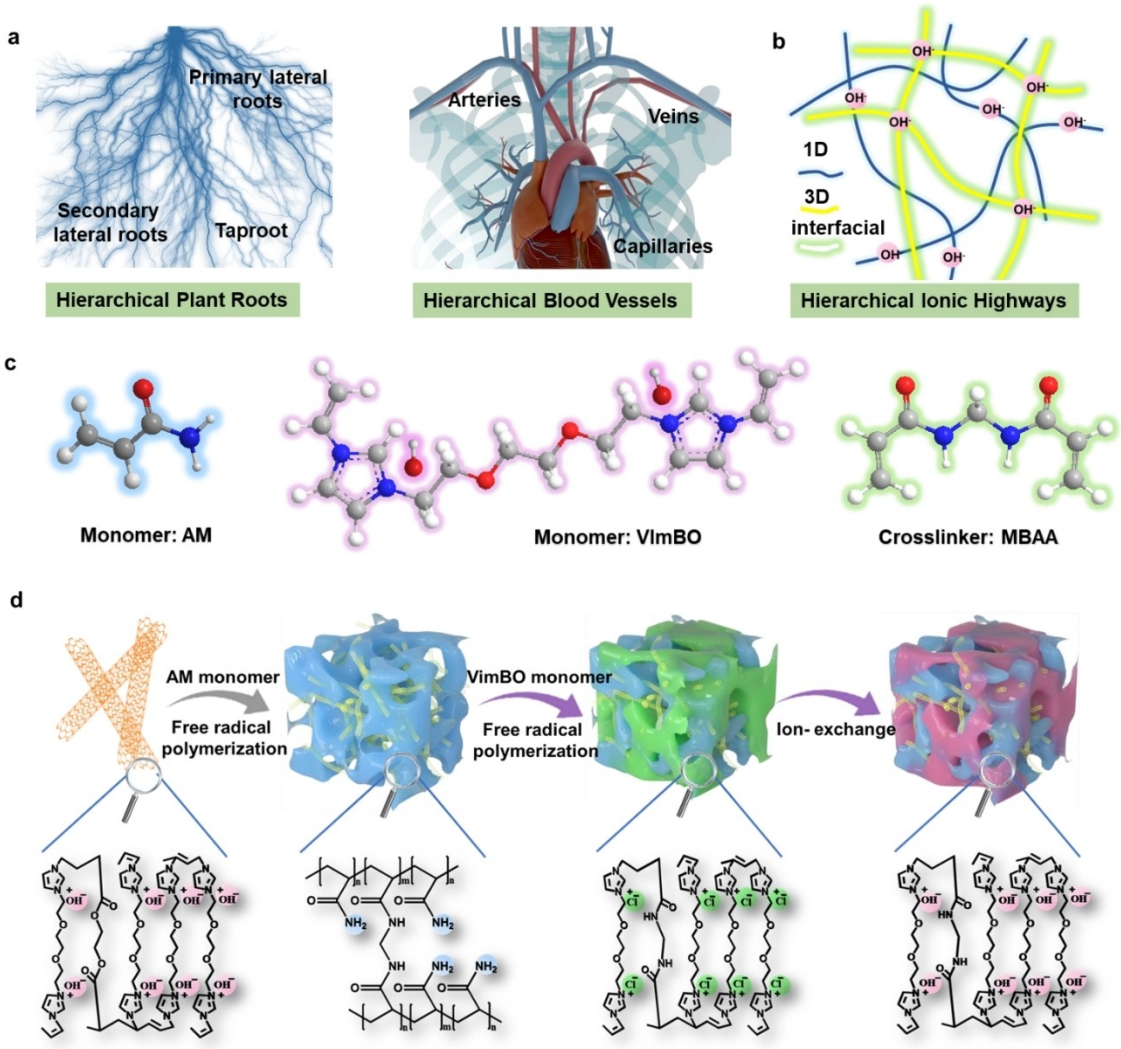

Figure 1. Design and fabrication of single-anion conductive SSEs with hierarchical ionic highways. (a) Hierarchical transport highways within plant roots and blood circulatory system. (b) Hierarchical ionic highways of SSEs for OH^- conduction: 3D highway, 1D highway and interfacial highway. (c) Chemical structure of VImBO monomer, AM monomer and crosslinker. (d) Fabrication of FCNT/PAM-PVImBO SSEs and the chemical structures of dual-penetrating networks.

dendrite growth on the Zn anode. The assembled flexible zinc-air batteries demonstrate a high-power density of 152 $mW \cdot cm^{-2}$ and a superlong lifetime over 350 hours, which outstrips most of the state-of-the-art flexible zinc-air batteries.[19]

Results and Discussion

Design and Synthesis of SSEs

The fabrication of SSEs comprises three steps: synthesis of FCNTs, synthesis of FCNT/PAM matrix, synthesis of SSEs with dual-penetrating networks (Figure 1d, experimental details in the Supporting Information). Firstly, VImBO monomer synthesized by a facile quaternary ammonium reaction is acted as both building block for construction of the intrinsic OH^--conductive ionomer and dressing agent for the surface modification of CNTs (Figure S2), and then FCNT is fabricated with distillation precipitation polymerization of VImBO monomer and cross-linker on the surface of the vinyl groups grafted CNTs (Figure S3). Compared with other grafting modifications, distillation precipitation polymerization easily generates a uniform and tailorable polymeric shell on the surface of CNT, thus contributing to the formation of abundant aggregations of OH^--conductive groups along the CNT surface. Secondly, free radical polymerization of acrylamide monomer and cross-linker is induced in the attendance of FCNT to fabricate hybrid FCNT/PAM matrix (Figure S4). Finally, single-anion conductive FCNT/PAM-PVImBO SSEs with good flexibility are constructed by in situ polymerization of VImBO monomer within the hybrid FCNT/PAM matrix to form dynamical dual-penetrating networks (Figure S5). FCNT/PAM-PVImBO SSEs easily achieve the synergistic advantages of polymer network (PAM) and ionomer network (PVImBO), which allows precise manipulation of polymer structures to realize high ion conductivity, good water retention and mechanical robustness simultaneously. The distinct hierarchical ionic highways consisting of 3D highway, 1D highway and interfacial highway afford high OH^- conductivity. The hydrophilic alkoxy groups and charged cations/anions of PVImBO and highly polar amide groups of PAM network possess high affinity towards water molecules, thus rendering the SSEs with good water uptake and retention. Moreover, the covalent and physical cross-linking as well as the entanglement of polymer chains endow the resultant SSEs excellent mechanical properties to tolerate routine deformations.

Physicochemical Characterizations

High-resolution transmission electron microscope (HRTEM) images clearly suggest CNTs are uniformly covered by PVImBO with shell thickness of 20 nm after distillation precipitation polymerization (Figure 2a–c, S6), and the well distribution of C, N, O, Cl (Figure 2d, S7) further confirms the successful fabrication of FCNTs with abundant OH^--conductive groups. The optical images of the

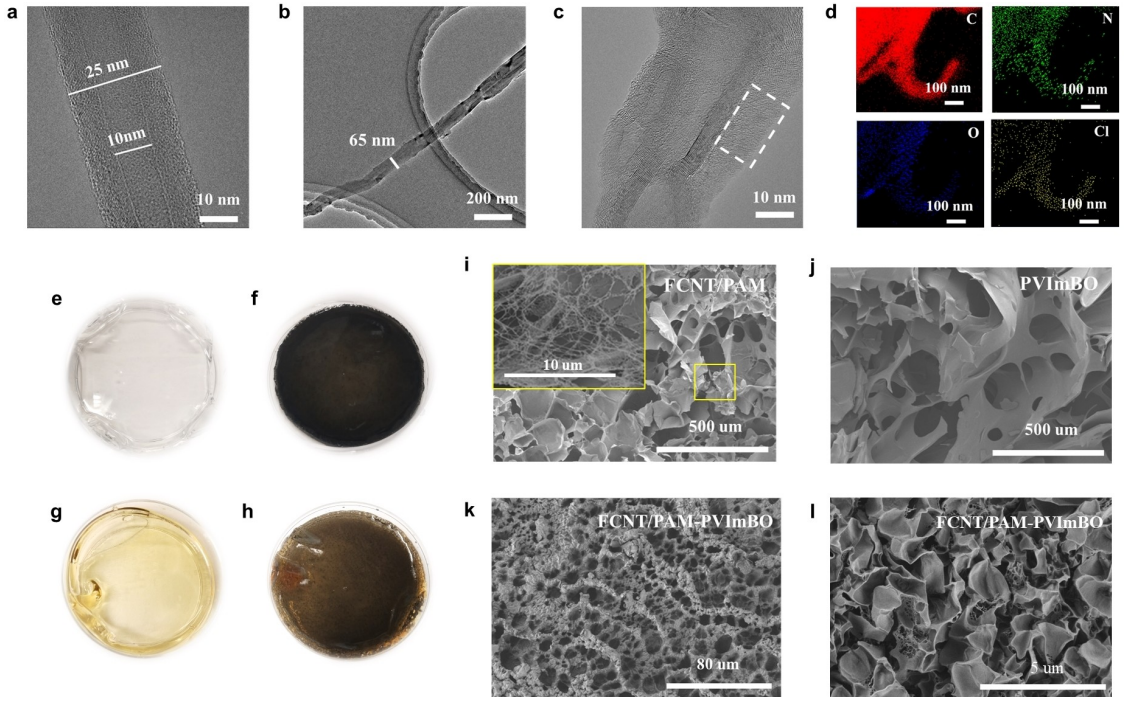

Figure 2. Morphology characterizations of SSEs. (a) HRTEM image of CNTs. (b–d) TEM and HRTEM images of FCNTs, and the corresponding EDS mapping of FCNTs. (e–h) Photos of PAM hydrogel, FCNT/PAM hydrogel, PVImBO ionic gel, and SSE. (i) Surface SEM images of freeze-dried FCNT/PAM hydrogel and the highlighted 1D ionic highways created by the embedded FCNTs. (j) Surface SEM image of freeze-dried PVImBO ionic gel. (k) Surface SEM image of freeze-dried SSE. (l) Cross-section SEM image of freeze-dried SSE.

PAM hydrogel, FCNT/PAM hydrogel, PVImBO ionic gel and SSE in Figure 2e–h and Figure S8 display thin flexible films with uniform shape and color. The micro-morphology of SSE and their morphology evolution in relative to PAM hydrogel and PVImBO ionic gel are observed by SEM, where all the samples with same water uptake of 20 $g \cdot g^{-1}$ are freeze-dried for SEM observations. Figure S9a highlights the well-defined 3D porous network structure of freeze-dried PAM hydrogel composed of abundant interconnected macropores with relatively uniform pore size distribution. Freeze-dried FCNT/PAM hybrid hydrogel exhibits the similar 3D porous network (Figure 2i), and FCNTs are mainly distributed within or anchored on the PAM walls to form cobweb-like structure due to the strong non-covalent interactions between FCNT and PAM (insert Figure). The distribution of FCNTs not only enhances the mechanical robustness but also renders the PAM with ion conductivity benefiting from the formation of 1D ion-conductive highways. The freeze-dried PVImBO ionic gel exhibits less but ultra-large disorderly arranged macropores, which suggests their overhydrated polymeric chains due to high water affinity of the hydrophilic alkoxy groups and high-density charged cations/anions (Figure 2j). In contrast, SSEs possess more regular and interconnected 3D porous structure, where plenty of smaller pores with size of several microns are uniformly distributed within the ordered polymeric ridges (Figure 2k–l, S9). Compared with FCNT/PAM and PVImBO, the number of pores within SSEs increases significantly, which indicates the formation of narrower and more unform water channels induced by PVImBO.

The crystalline structures of hot-dried SSEs, PAM, FCNT/PAM and PVImBO are studied by X-ray diffraction (XRD), which suggests their amorphous structure (Figure 3a). The XRD pattern of PAM witnesses a broad and pronounced peak at $2\theta = 25.0°$ and a shoulder peak at $2\theta = 37.0°$. The peak intensity dramatically decreases for FCNT/PAM, which indicates that the impregnation of FCNTs blocks the orderly arrangement of PAM polymer chains. As for PVImBO, no observation of apparent peak indicates the completely amorphous structure, which is expected as good conductor for OH^- conduction. As expected, hot-dried and wet SSEs exhibit both amorphous structure, which suggests

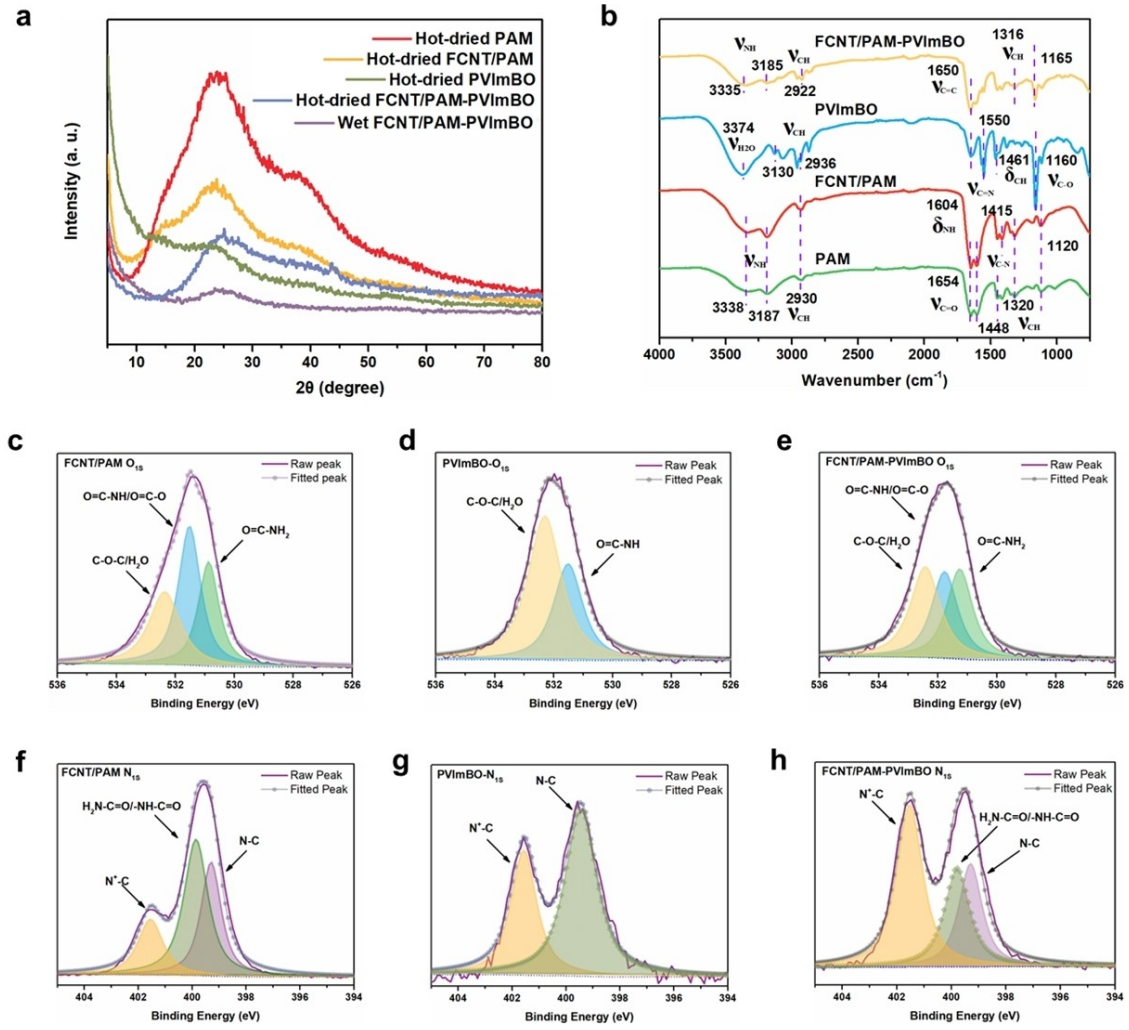

Figure 3. Chemistry characterizations of SSE. (a) XRD patterns of hot-dried FCNT/PAM-PVImBO SSEs. (b) ATR-FTIR spectra of freeze-dried FCNT/PAM-PVImBO SSEs. (c–h) Deconvoluted XPS spectra of FCNT/PAM, PVImBO, and FCNT/PAM-PVImBO SSEs in the O1s and N1s regions.

superhigh chain mobility, thus contributing to excellent ion conductivity with low energy barrier.

The chemistry of SSEs such as chemical synthesis and molecular interactions are investigated by proton nuclear magnetic resonance (^{1}H NMR) and attenuated total reflectance-Fourier transform infrared spectroscopy (ATR-FTIR). In H NMR spectrum, the observations of chemical shifts ascribed to vinyl imidazole cations and alkoxy linker confirm the successful synthesis of VImBO monomer (Figure S10). FTIR spectra further confirms the successful chemical synthesis of VImBO monomer and FCNTs (Figure S11). The characteristic peaks assigned to CNTs disappear or are weakened, while a new characteristic peak of vinyl group at 1632 cm^{-1} appears, indicating the effective surface modification by silane coupling agent. Moreover, the characteristic peaks of PVImBO appearing in FCNTs suggests the successful coverage of PVImBO on CNTs by distillation precipitation polymerization. As seen from Figure 3b and Figure S12, the ATR-FTIR spectrum of SSEs integrates the characteristic peaks of both PAM and PVImBO such as NH_2 stretching vibration peaks of PAM at 3335 cm^{-1} and 3185 cm^{-1}, C=C stretching vibration peak of PVImBO at 1316 cm^{-1}, and C=N stretching vibration peak of PVImBO at 1550 cm^{-1}, which verify the dynamical dual-penetrating networks. However, some peaks of SSEs exhibit red-shifts or bule shifts in relative to pristine PAM and PVImBO, which indicates the intramolecular interactions are weakened and intermolecular interactions such as hydrogen-bond interactions and electrostatic interactions are formed due to the intertwining of polymer chains from PAM and PVImBO.

The chemical compositions of SSEs are further explored by X-ray photoelectron spectroscopy (XPS). The XPS survey spectrum of SSE displays four peaks with binding energies at 284.8 eV, 399.5 eV, 531.8 eV, and 197.1 eV, which are attributed to C1s, N1s, O1s, and Cl2p (Figure S13). The C/O atomic ratio of SSE is 6.5, which locates between that of PAM (3.1) and PVImBO (8.3), suggesting that plenty of PVImBO chains are distributed on the surface of SSEs. Moreover, the chemical statuses of C, O and N are further revealed by the high-resolution XPS spectra (Figure 3c–h, S14). Compared with pristine FCNT/PAM hydrogel, the peak of O=C–NH_2 of SSEs in the O1s spectrum shifts to a higher binding energy from 530.8 eV to 531.3 eV, which suggests the decreased electron cloud density of O atom due to the formation of hydrogen bonding or electrostatic interactions between C=O chain and imidazole dual-cations of PVImBO chain. As for the N1s spectra, the N chemical statuses of the PVImBO and PAM are completely different with huge binding energy difference at 401.5 eV and 399.5 eV, which are related to quaternary C–N^+ cation and C–N bond. The N1s XPS spectrum of SSE further highlights the its synergy of polymer and ionomer.

Comprehensive Properties of SSEs

Structure design and molecular synthesis render the SSEs with fascinating comprehensive properties. SSEs can be easily processed into arbitrary shapes to satisfy different battery configurations (Figure S15). Particularly, SSEs exhibit adhesion towards carbon cloth and stainless-steel cloth under a drawing force (Figure 4a), favoring the intimate electrolyte/electrode interface. Moreover, SSEs can withstand high-level deformations of bending (Figure 4b), compressing, recovery (Figure 4c, S16), stretchability (Figure 4d), and twisting (Figure 4e). The maximum elongation reaches up to 1200 % with fast self-recovery. As certified by quantitative stress-strain measurements (Figure 4f), PVImBO ionic gel shows poor mechanical property with tensile stress of 11.5 kPa, and PAM hydrogel obtains the maximum strain of 970 % and tensile stress of 130 kPa. However, the PAM hydrogel almost loses all the mechanical robustness (115 % and 20 kPa) after incorporation of 6 mol/L KOH solution due to the severe destroy of molecular interactions. Impressively, the as-designed SSE is easily stretched to about 1200 % strain with tensile stress of 180 kPa, which is about 15 times higher than that of PVImBO ionic gel. Moreover, the structure stability of SSEs is confirmed by the relatively constant stress-strain curves over a long period measurement (Figure S17), and their good self-recovery is certified by successive cyclic stretching measurement at maximum stretchability of 300 % and 500 % (Figure S18, S19). The super-stretchability and toughness of FCNT/PAM-PVImBO SSEs is mainly originated from the dynamical dual-penetrating networks with the synergy of a highly cross-linked rigid PVImBO ionomer and a loosely cross-linked soft PAM polymer, where abundant chemical cross-linking and physical interactions are generated and effectively dissipate the deformation energy. Especially, hydrogen bonding or electrostatic interactions can dynamically break and reform during strain, and the dynamic intertwining of polymer chains also increases the flexibility of SSEs through chain sliding.

Water retention and uptake also determine the battery life due to the half-open system of zinc-air battery. The SSEs have a superb water retention capability with a water retention of 95.3 % and 83.5 % for 12 hours and 200 hours, which is much higher than traditional PVA hydrogel (12.5 % for 200 hours) and very competitive compared to PAM gel electrolyte (Figure S20). As for traditional GPEs, the KOH precipitations easily crystallize out upon water evaporation, which damages electrolyte/electrode interface (Figure S21). As expected, the SSE obtains a water uptake of 153.6 $g \cdot g^{-1}$ at equilibrium state due to their porous structure as well as plenty of cations/anions and highly polar groups (Figure 4g), which is two orders of magnitude higher than PVA hydrogel and GPEs (1.5 $g \cdot g^{-1}$ and 1.2 $g \cdot g^{-1}$). The real-time water-uptake curves suggest the moderate water absorption rate of SSEs (Figure S22), which is much faster than PVA and PAM hydrogel but slightly slower than PVImBO ionic gel.

SSEs exhibit good ion conductivities of 245 $mS \cdot cm^{-1}$, 149 $mS \cdot cm^{-1}$ and 94 $mS \cdot cm^{-1}$ at water uptake of 1 $g \cdot g^{-1}$, 5 $g \cdot g^{-1}$ and 10 $g \cdot g^{-1}$ (Figure S23). The decrease of ion conductivity is attributed to the lessened concentration of OH^- with the increase of water content, where the ion conductivity of SSEs originates from intrinsic OH^- ions of ionomer rather than the embedded KOH solution like

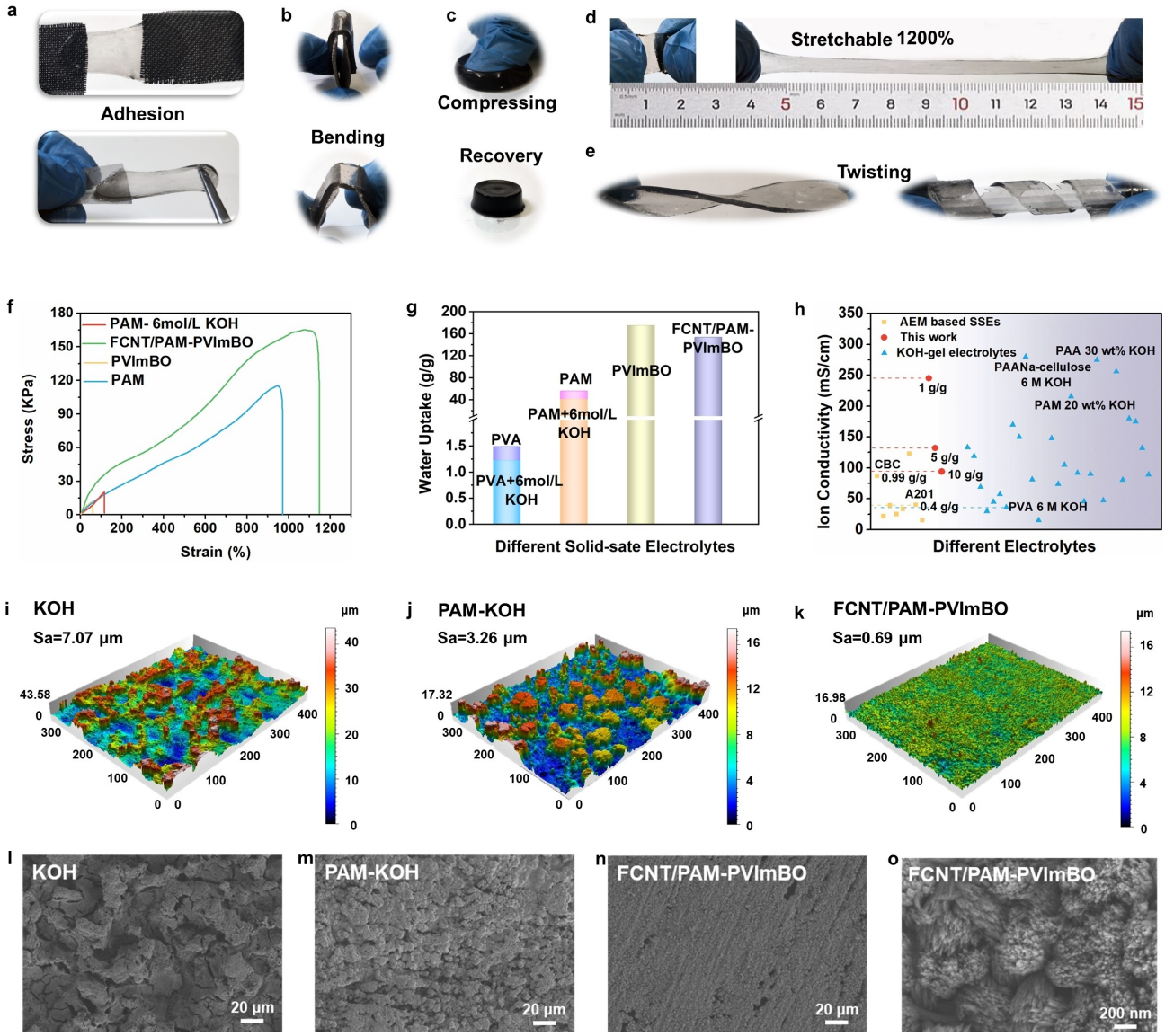

Figure 4. Excellent comprehensive properties of SSEs. (a) Adhesion of SSEs to carbon cloth and stainless-steel cloth to create intimate electrolyte/electrode interface. (b–e) Mechanical robustness of SSEs with toleration to routine deformations including bending, compressing, recovery, 1200% stretchability and twisting. (f) Tensile stress-strain curves of PAM hydrogel, PAM hydrogel electrolyte, PVImBO ionic gel, and SSEs with water uptake of 10 g/g. (g) Comparison of ultimate water uptakes of PVA hydrogel, PAM hydrogel, PVImBO ionic gel and SSEs. (h) Comparison of ion conductivity of SSEs with previously reported GPEs and AEMs for zinc-air batteries. (i–k) LCSM images and the corresponding surface roughness of Zn anodes after 50 cycles with KOH electrolyte (2 mol/L), PAM-KOH GPE and SSE. (l–o) SEM images of Zn anodes after 50 cycles with KOH electrolyte (2 mol/L), PAM-KOH GPE and SSE.

GPEs. The ion conductivity of SSEs is higher than most of GPEs but slight lower than the advanced GPEs based on highly concentrated KOH solution (Table S1). Fortunately, the hierarchical ionic highways and high ion density endow SSEs with competitive ion conductivity even under high water uptake. The ion conductivity of SSEs at 1 $g \cdot g^{-1}$ is almost an order of magnitude higher than that of A201 membrane or PVA GPE (Figure 4h), and the ion conductivity of SSE at 5 $g \cdot g^{-1}$ is higher than all the reported the state-of-the-art AEMs. Considering the excellent comprehensive properties of SSEs and their safety without highly corrosive KOH, the as-designed SSEs are very promising for flexible zinc-air batteries.

Moreover, the as-designed SSEs significantly promote the reversibility of Zn anode. The morphology of Zn anodes after 50 cycles with SSEs is explored by laser confocal scanning microscopy (LCSM) and SEM. 3D LCSM images clearly indicates that SSEs can suppress the dendrite growth and corrosion reaction on the Zn anode compared with KOH electrolyte. Zn anode in KOH electrolyte shows an obvious dendrite-like surface with the largest average surface roughness of 7.07 μm (Figure 4i). In sharp comparison, a flat and dendrite-free surface with an average surface

roughness of 0.69 μm is observed for Zn anode with FCNT/PAM-PVImBO SSE, which is also much lower than that of the most widely used PAM GPE (Figure 4i–k, S24). As further confirmed by SEM images (Figure 4l–o, S25), the Zn anode cycled in KOH electrolyte is overgrown with the scattered micrometer-sized protrusions, valley and cracks. PAM-KOH GPE can relieve the dendrite growth and corrosion reaction, but still results in the rough Zn anode with irregular clusters. In contrast, Zn anode with FCNT/PAM-PVImBO SSE displays the smooth and dense surface with the uniform distribution of nanometer-sized sprout-like deposits, showing that dendrites and corrosion reactions are greatly inhibited.

Visualization of Hierarchical Ionic Highways

Hierarchical ionic highways are visualized by atomistic molecular dynamics (MD) simulation.[20] The bulk structure of PVImBO shows nanophase segregation morphology with water-accessible surface (Figure 5a–b). During MD annealing, the OH^- and water assemble into 3D well-connected hydrophilic domains, while entangled polymer framework are aggregated into hydrophilic domains (Figure 5c–d, S26).[21] The imidazolium cations pack themselves to hydrophilic domains, which act as hopping sites for OH^- conduction, thus affording high ion conductivity and fast reaction kinetics. The self-aggregation of PVImBO polymer is weakened and becomes more structured with the stretched chains at high hydrated state. The nanophase segregation morphology with alternating hydrophobic and

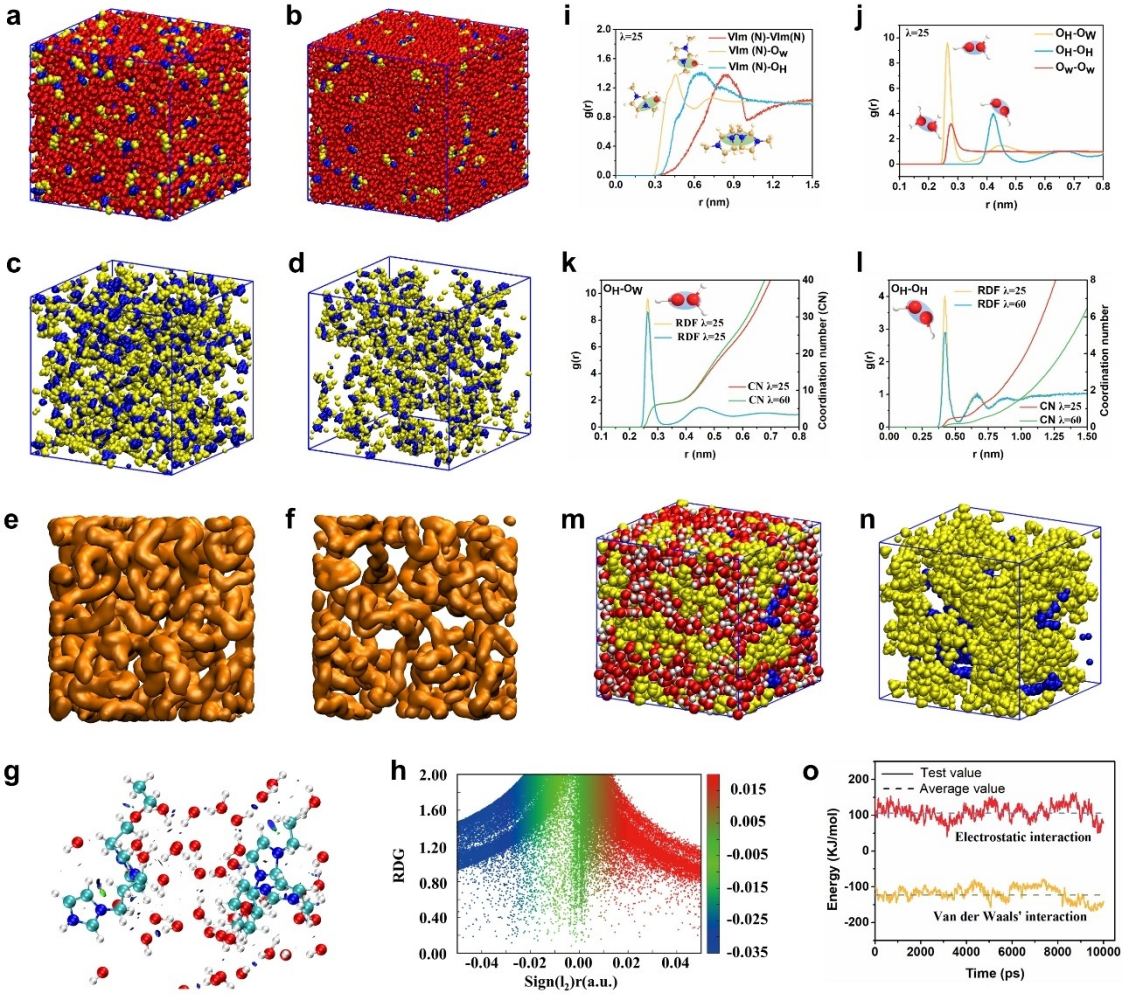

Figure 5. Visualization of hierarchical ionic highways. (a, b) Bulk structure of PVImBO at hydrated states (λ) of 25 and 60. (c, d) Self-aggregations of PVImBO polymer chain with dual-cation in blue and alkoxy linker in yellow at λ of 25 and 60. (e, f) 3D highway for OH^- diffusion highlighted by iso-surface of PVImBO polymer chains at λ of 25 and 60. (g) Solvated structure of PVImBO polymer chain at λ of 25. (h) Plots of the reduced density gradient versus the electron density multiplied by the sign of the second Hessian eigenvalue. (i-l) Radial distribution functions (RDF) and coordination numbers (CN): (i) RDF of imidazolium cation-imidazolium cation, imidazolium cation-water and imidazolium cation-OH^-; (j) RDF of OH^--water, water-water, and OH^-–OH^-; (k) RDF and CN of OH^-–OH^- at λ of 25 and 60. (l) RDF and CN of OH^-–H_2O at λ of 25 and 60. (m, n) Bulk structure of interfacial highway. (o) Binding energy and molecular interactions between PVImBO polymer chain and PAM chain under hydrated state.

hydrophilic domains are robust accompanying with dynamic reconfiguration topology and the expanded hydrophilic domains, which contribute to maintaining relatively high ion conductivity. The iso-surface mappings offer a more global visual impression of better 3D highways for OH^- conduction, which are more uniform in size and more connected with each other in comparison to the discrete ionic clusters and bottleneck-like connection between ionic clusters in traditional AEMs (Figure 5e–f).[22] As seen from Figure 5g, both cations and alkoxy linker intrinsically coordinate with H_2O molecules and hydrated OH^-, which render the SSE with high water uptake and plenty of active sites for OH^- conduction, thus extending the ion conduction region from the cations to the whole polymer chain for obtaining high ion conductivity. The reduced density gradient scatter (Figure 5h, S27) highlights the molecular interactions for driving nanophase segregation, including the hydrogen-bond interactions, electrostatic interactions and Van der Waals interactions.

The local structure of 3D highways is further described by radial distribution function (RDF) and coordination number (CN) (Figure 5i–l).[23] The imidazolium cation and OH^- prefer to be solvated by water molecules, which protects imidazolium cation from nucleophilic attack by OH^- to obtain structural stability (Figure 5i–j, S28). The overlapping first solvation shell of imidazolium cations contributes to the formation of successive 3D highways (Figure S29), the dual-cation molecular design and complete solvation of cation result in pronounced peak and high CNs at both low and high hydrated states, which contribute to the shorter distance for fast OH^- conduction in relative to traditional AEMs. As highlighted in Figure 5k–l and Figure S30, the overlap of OH^- solvation shell and well-organized water belt like bulk-water phase means the good development of hydrogen-bonding network, thus further contributing to the fast OH^- conduction. The snapshots of OH^- conduction via the 3D highways are shown in Figure S31 and the OH^- self-diffusion coefficient are much higher than traditional AEMs (Table S2). Finally, the visualization of interfacial highways suggestes the intertwined morphology due to the molecular interactions between the PAM polymer chain and PVImBO chain (Figure 5m–n, S32). Some solvated OH^- escape the constraint by imidazolium cation and embrace PAM chain, which results in the OH^- distribution throughout the polymer interphase, contributing to the high ion conductivity. The negative total binding energy without considering hydrogen-bond interactions suggests interfacial compatibility between polymer chains and contributes to relatively compact interfacial highways for the fast OH^- conduction.

Flexible Solid-State Zinc-air Batteries

Flexible zinc-air batteries are assembled by sandwiching the SSE between bifunctional Pt/C–Co_3O_4 loaded air cathode and zinc foil or zinc-electrodeposited carbon cloth (Figure 6a, S33, S34). For comparison, flexible zinc-air batteries utilizing commercial A201 membrane and traditional PVA GPE are also fabricated following the same procedure. The flexible zinc-air battery with SSEs provides an open circuit voltage of 1.47 V and 2.92 V in series (Figure S35), which are much higher than that of PVA or A201 based batteries (1.36 V and 1.32 V). The specific capacity (normalized to the mass of the zinc electrode) of a primary zinc-air battery with SSE is 764 $mAh \cdot g^{-1}$ at the current density of 2 $mA \cdot cm^{-2}$ (Figure 6b), and the corresponding energy density is 970 $Wh \cdot kg^{-1}$, which significantly surpasses PVA and A201 based batteries (468 and 315 $mAh \cdot g^{-1}$). At current density of 5 $mA \cdot cm^{-2}$, the SSE based zinc-air battery still maintains a high specific capacity of 733 $mAh \cdot g^{-1}$. Figure 6c displays the higher and more stable discharge plateaus of SSE based zinc-air battery at different current densities compared with PVA and A201 based batteries, whose performances severely deteriorates at the current density higher than 5 $mA \cdot cm^{-2}$. The SSE based zinc-air battery presents stable discharge plateaus even at current density of 10 $mA \cdot cm^{-2}$ and good recovery, which further suggests its excellent rate performance. Due to high ion conductivity and intimate electrolyte-electrode interface, the zinc-air battery assembled with SSEs delivers a narrower charge–discharge voltage gap at a broad range of current density compared with PVA and A201 based batteries (Figure 6d). The corresponding peak power density reaches up to 152 $mW \cdot cm^{-2}$ (Figure 6e), which is substantially enhanced in relative to those of A201 based battery (30 $mW \cdot cm^{-2}$) and PVA based battery (38 $mW \cdot cm^{-2}$). The key performance parameters of SSE based zinc-air battery outperforms the controlled batteries based on A201 and PVA, especially for cycling time (Figure 6f). As further highlighted by

Figure 6g, the SSE based zinc-air battery is stably charged and discharged up to 1050 cycles for 350 hours, while the controlled batteries assembled with A201 and PVA deliver the stable discharge-charge curves only for 20 hours and 33 hours (Figure S36). The morphology of Zn anode after cycling is shown in Figure S37. A degraded surface with severe corrosion is found after repeated plating/stripping, indicating that the battery failure may caused by the unstable electrolyte interface, which emphasizs that synergies between surface treatment of Zn anode and electrolyte design to obtain the satisfactory performance for practical application of zinc-air battery.[24] The SSE based zinc-air battery witnesses a negligible increases of voltage gap from 0.78 V to 0.85 V after 350 hours, which represents an excellent cycling stability with the extremely low voltage fading rate of 0.067 mV per cycle. In comparison, the voltage gaps of PVA and A201 based batteries significantly soar to 1.4 V and 1.8 V after 30 and 20 hours, respectively. The excellent cycling lifespan of zinc-air batteries mainly profit from the high ion conductivity and good water retention of SSEs. As seen from Figure 6h, the power density and cycling lifespan of SSE based zinc-air battery are an order of magnitude higher than those of all the reported batteries based on the state-of-the-art AEMs, and exceeds most of batteries based on the advanced KOH based GPEs. The comparison in term of discharge voltage and specific capacity further highlights the excellent performance of SSE based zinc-air batteries, which validates the application of

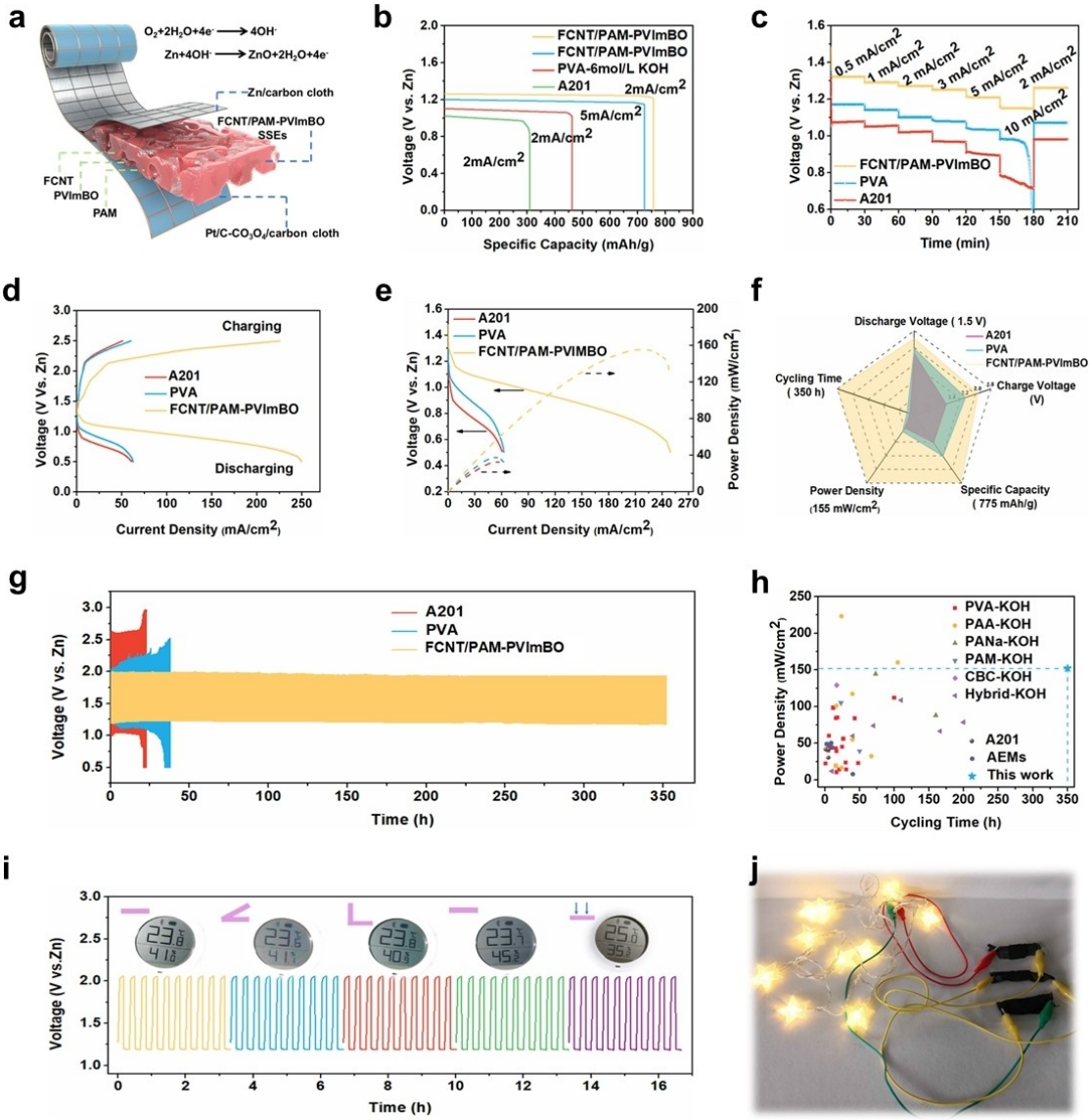

Figure 6. Electrochemical performance of flexible zinc-air batteries assembled with SSE, A201 and PVA. (a) Schematic illustration of sandwich configuration of flexible zinc-air battery. (b) Specific capacity curves. (c) Discharge plateaus at different current densities. (d, e) Charge and discharge polarization curves, and the corresponding power density curves. (f) Comprehensive comparison of key parameter of batteries. (g) Galvanostatic cycling stability of zinc-air batteries at current density of 2 mA·cm^{-2} with per cycle of 20 minutes. (h) Comparison of power density and cycling time of SSE based zinc-air battery with previously reported solid-state zinc-air batteries during past two decades. (i) Galvanostatic charge and discharge cycle curves of the zinc-air battery under different bending conditions. (j) Three zinc-air batteries in series as power supply for a festival lamp.

the as-designed SSEs for solid-state zinc-air battery (Figure S38). As a proof of concept, the flexibility of SSE based zinc-air battery is elevated under different bending angles. The flexible zinc-air battery delivers very stable charge and discharge voltages without any notable performance degradation, and the hygrometer can work well when the battery is subject to the gradual increase of bending angles (Figure S39). The superior mechanical flexibility and stable performance can be credited to the excellent flexibility, and satisfying mechanical robustness of SSEs, as well as favorable adhesiveness towards electrodes. More practically, three flexible zinc-air batteries connected in series can power a yellow a festival lamp, suggesting their potential practical applications as a flexible power source (Figure 6j).

Conclusion

In summary, we have developed a safe and single-anion conductive SSEs for flexible zinc-air batteries, which is constructed by incorporating PVImBO ionomer within the robust FCNT/PAM hybrid matrix. The ion conductivity of SSE depends on the abundant intrinsic OH^- ions of PVImBO ionomer rather than the doped concentrated

KOH solution, excluding the safety hazard of corrosive damage associated with most traditional GPEs due to KOH leakage. The hierarchical ionic highways consisting of 3D highway, 1D highway and interfacial highway afford high OH^- conductivity of 245 $mS \cdot cm^{-1}$, which is one order of magnitude higher than previous AEMs. Meanwhile, the dual-penetrating ionomer-polymer networks result in mechanical robustness of SSEs with toleration to routine deformations of bending, compressing, recovery, 1200 % stretch-ability and twisting. The as-fabricated SSE is also featured with decent water and retention, which is almost 100 times higher than commercial A201 membrane and reported AEMs. The visualization of hierarchical ionic highways by molecular dynamics suggests that the molecular design of dual-cation and high chain flexibility render the SSEs with plenty of sites and uniform and connected highways for OH^- conduction. The flexible solid-state zinc-air batteries assembled with SSEs exhibit superior electrochemical performance with high power density and specific capacity, and ultralong cycling stability for over 350 hours, outperforming most of the state-of-the-art flexible zinc-air batteries. In addition, possibilities exist for increasing the electrochemical performance and lifespan of flexible zinc-air batteries by using home-made bifunctional catalyst and commercial encapsulation techniques, but the safe and single-anion conductive SSEs proposed here broadens the definition and scope of OH^- conductors, and the hierarchical ionic highways and in-depth insight of ion conduction mechanism may guide us in developing highly conductive SSEs for energy-storage devices.

Acknowledgements

This work is supported by the Energy Revolution S&T Program of Yulin Innovation Institute of Clean Energy, Grant No.YIICE E411060316. Thanks for the support of the Strategic Priority Research Program of the Chinese Academy of Sciences (Grant No: XDB0600000, XDB0600200) and the Postdoctoral Fellowship Program of CPSF (GZB20230726).

Conflict of Interest

The authors declare no conflict of interest.

Data Availability Statement

The data that support the findings of this study are available from the corresponding author upon reasonable request.

Keywords: zinc-air battery · solid-state electrolyte · single-anion conduction · dual-penetrating networks · hierarchical ionic highway

[1] a) X. Zhong, Y. Shao, B. Chen, C. Li, J. Sheng, X. Xiao, B. Xu, J. Li, H.-M. Cheng, G. Zhou, *Adv. Mater.* **2023**, *35*, 2301952; b) J. Cai, H. Zhang, L. Zhang, Y. Xiong, T. Ouyang, Z.-Q. Liu, *Adv. Mater.* **2023**, *35*, 2303488; c) X. Zeng, K. Xie, S. Liu, S. Zhang, J. Hao, J. Liu, W. K. Pang, J. Liu, P. Rao, Q. Wang, J. Mao, Z. Guo, *Energy Environ. Sci.* **2021**, *14*, 5947–5957.

[2] a) S. S. Shinde, J. Y. Jung, N. K. Wagh, C. H. Lee, D.-H. Kim, S.-H. Kim, S. U. Lee, J.-H. Lee, *Nat. Energy* **2021**, *6*, 592–604; b) W. Li, B. Liu, D. Liu, P. Guo, J. Liu, R. Wang, Y. Guo, X. Tu, H. Pan, D. Sun, F. Fang, R. Wu, *Adv. Mater.* **2021**, *35*, 2109605; c) M. Cui, N. Ma, H. Lei, Y. Liu, W. Ling, S. Chen, J. Wang, H. Li, Z. Li, J. Fan, Y. Huang, *Angew. Chem. Int. Ed.* **2023**, *62*, e202303845.

[3] a) J.-N. Liu, C.-X. Zhao, J. Wang, D. Ren, B.-Q. Li, Q. Zhang, *Energy Environ. Sci.* **2022**, *15*, 4542–4553; b) Y. Zhang, Y.-P. Deng, J. Wang, Y. Jiang, G. Cui, L. Shui, A. Yu, X. Wang, Z. Chen, *Energy Storage Mater.* **2021**, *35*, 538–549; c) C.-X. Zhao, J.-N. Liu, J. Wang, C. Wang, X. Guo, X.-Y. Li, X. Chen, L. Song, B.-Q. Li, Q. Zhang, *Sci. Adv.* **2022**, *8*, eabn5091.

[4] A. I. Douka, Y. Xu, H. Yang, S. Zaman, Y. Yan, H. Liu, M. A. Salam, B. Y. Xia, *Adv. Mater.* **2020**, *32*, 2002170.

[5] a) W. Sun, F. Wang, B. Zhang, M. Zhang, V. Küpers, X. Ji, C. Theile, P. Bieker, K. Xu, C. Wang, M. Winter, *Science* **2021**, *371*, 46–51; b) C.-X. Zhao, J.-N. Liu, N. Yao, J. Wang, D. Ren, X. Chen, B.-Q. Li, Q. Zhang, *Angew. Chem. Int. Ed.* **2021**, *60*, 15281–15285; c) C.-Y. Chen, K. Matsumoto, K. Kubota, R. Hagiwara, Q. Xu, *Adv. Energy Mater.* **2019**, *9*, 1900196.

[6] a) X. Fan, R. Zhang, S. Sui, X. Liu, J. Liu, C. Shi, N. Zhao, C. Zhong, W. Hu, *Angew. Chem. Int. Ed.* **2023**, *62*, e202302640; b) X. Fan, H. Wang, X. Liu, J. Liu, N. Zhao, C. Zhong, W. Hu, J. Lu, *Adv. Mater.* **2023**, *35*, 2209290; c) Y. Huang, Z. Li, Z. Pei, Z. Liu, H. Li, M. Zhu, J. Fan, Q. Dai, M. Zhang, L. Dai, C. Zhi, *Adv. Energy Mater.* **2018**, *8*, 1802288; d) Z. Pei, Z. Yuan, C. Wang, S. Zhao, J. Fei, L. Wei, J. Chen, C. Wang, R. Qi, Z. Liu, Y. Chen, *Angew. Chem. Int. Ed.* **2020**, *59*, 4793–4799; e) J. Park, M. Park, G. Nam, J.-s. Lee, J. Cho, *Adv. Mater.* **2015**, *27*, 1396–1401.

[7] M. Jiao, L. Dai, H.-R. Ren, M. Zhang, X. Xiao, B. Wang, J. Yang, B. Liu, G. Zhou, H.-M. Cheng, *Angew. Chem. Int. Ed.* **2023**, *62*, e202301114.

[8] a) Z. Pei, L. Ding, C. Wang, Q. Meng, Z. Yuan, Z. Zhou, S. Zhao, Y. Chen, *Energy Environ. Sci.* **2021**, *14*, 4926–4935; b) T. Cui, Y.-P. Wang, T. Ye, J. Wu, Z. Chen, J. Li, Y. Lei, D. Wang, Y. Li, *Angew. Chem. Int. Ed.* **2022**, *61*, e202115219; c) H. Tian, A. Song, P. Zhang, K. Sun, J. Wang, B. Sun, Q. Fan, G. Shao, C. Chen, H. Liu, Y. Li, G. Wang, *Adv. Mater.* **2023**, *35*, 2210714.

[9] a) Y. Zhou, J. Pan, X. Ou, Q. Liu, Y. Hu, W. Li, R. Wu, J. Wen, F. Yan, *Adv. Energy Mater.* **2021**, *11*, 2102047; b) N. Xu, Y. Zhang, M. Wang, X. Fan, T. Zhang, L. Peng, X.-D. Zhou, J. Qiao, *Nano Energy* **2019**, *65*, 104021; c) W. Wang, M. Tang, Z. Zheng, S. Chen, *Adv. Energy Mater.* **2019**, *9*, 1803628; d) J. Zhang, J. Fu, X. Song, G. Jiang, H. Zarrin, P. Xu, K. Li, A. Yu, Z. Chen, *Adv. Energy Mater.* **2016**, *6*, 1600476.

[10] a) J. Fu, J. Zhang, X. Song, H. Zarrin, X. Tian, J. Qiao, L. Rasen, K. Li, Z. Chen, *Energy Environ. Sci.* **2016**, *9*, 663–670; b) H. Dou, M. Xu, Z. Zhang, D. Luo, A. Yu, Z. Chen, *Adv. Mater. n/a*, 2401858; c) M. Wang, N. Xu, J. Fu, Y. Liu, J. Qiao, *J. Mater. Chem. A* **2019**, *7*, 11257–11264.

[11] a) L. Yang, H. Xiao, Y. Qian, X. Zhao, X.-Y. Kong, P. Liu, W. Xin, L. Fu, L. Jiang, L. Wen, *Nat. Sustain.* **2022**, *5*, 71–80; b) A. C. Yang, M. Y. Stevens, M. B. Chen, D. P. Lee, D. Stähli, D. Gate, K. Contrepois, W. Chen, T. Iram, L. Zhang, R. T. Vest, A. Chaney, B. Lehallier, N. Olsson, H. du Bois, R. Hsieh, H. C. Cropper, D. Berdnik, L. Li, E. Y. Wang, G. M. Traber,

C. R. Bertozzi, J. Luo, M. P. Snyder, J. E. Elias, S. R. Quake, M. L. James, T. Wyss-Coray, *Nature* **2020**, *583*, 425–430.
[12] a) K. A. McCulloh, J. S. Sperry, F. R. Adler, *Nature* **2003**, *421*, 939–942; b) X. Zheng, G. Shen, C. Wang, Y. Li, D. Dunphy, T. Hasan, C. J. Brinker, B.-L. Su, *Nat. Commun.* **2017**, *8*, 14921; c) M. Zhu, Y. Li, G. Chen, F. Jiang, Z. Yang, X. Luo, Y. Wang, S. D. Lacey, J. Dai, C. Wang, C. Jia, J. Wan, Y. Yao, A. Gong, B. Yang, Z. Yu, S. Das, L. Hu, *Adv. Mater.* **2017**, *29*, 1704107.
[13] a) H. Li, C. Han, Y. Huang, Y. Huang, M. Zhu, Z. Pei, Q. Xue, Z. Wang, Z. Liu, Z. Tang, Y. Wang, F. Kang, B. Li, C. Zhi, *Energy Environ. Sci.* **2018**, *11*, 941–951; b) U. G. K. Wegst, H. Bai, E. Saiz, A. P. Tomsia, R. O. Ritchie, *Nat. Mater.* **2015**, *14*, 23–36.
[14] a) M. Xu, H. Dou, Z. Zhang, Y. Zheng, B. Ren, Q. Ma, G. Wen, D. Luo, A. Yu, L. Zhang, X. Wang, Z. Chen, *Angew. Chem. Int. Ed.* **2022**, *134*, e202117703; b) D. Han, C. Cui, K. Zhang, Z. Wang, J. Gao, Y. Guo, Z. Zhang, S. Wu, L. Yin, Z. Weng, F. Kang, Q.-H. Yang, *Nat. Sustain.* **2021**, *5*, 205–213.
[15] Y. Zhu, L. Ding, X. Liang, M. A. Shehzad, L. Wang, X. Ge, Y. He, L. Wu, J. R. Varcoe, T. Xu, *Energy Environ. Sci.* **2018**, *11*, 3472–3479.
[16] X. Zhong, Z. Zheng, J. Xu, X. Xiao, C. Sun, M. Zhang, J. Ma, B. Xu, K. Yu, X. Zhang, H.-M. Cheng, G. Zhou, *Adv. Mater.* **2023**, *35*, 2209980.
[17] a) L. Ma, S. Chen, D. Wang, Q. Yang, F. Mo, G. Liang, N. Li, H. Zhang, J. A. Zapien, C. Zhi, *Adv. Energy Mater.* **2019**, *9*, 1803046; b) Q. Liu, C. Xia, C. He, W. Guo, Z. P. Wu, Z. Li, Q. Zhao, B. Y. Xia, *Angew. Chem. Int. Ed.* **2022**, *61*, e202210567.
[18] J. Ma, G. Zhong, P. Shi, Y. Wei, K. Li, L. Chen, X. Hao, Q. Li, K. Yang, C. Wang, W. Lv, Q.-H. Yang, Y.-B. He, F. Kang, *Energy Environ. Sci.* **2022**, *15*, 1503–1511.
[19] a) C. Hang, J. Zhang, J. Zhu, W. Li, Z. Kou, Y. Huang, *Adv. Energy Mater.* **2018**, *8*, 1703539; b) Y. Guo, P. Yuan, J. Zhang, Y. Hu, I. S. Amiinu, X. Wang, J. Zhou, H. Xia, Z. Song, Q. Xu, S. Mu, *ACS Nano* **2018**, *12*, 1894–1901; c) S. Peng, X. Han, L. Li, S. Chou, D. Ji, H. Huang, Y. Du, J. Liu, S. Ramakrishna, *Adv. Energy Mater.* **2018**, *8*, 1800612; d) C. Guan, A. Sumboja, H. Wu, W. Ren, X. Liu, H. Zhang, Z. Liu, C. Cheng, S. J. Pennycook, J. Wang, *Adv. Mater.* **2017**, *29*, 1704117; e) Y. Li, C. Zhong, J. Liu, X. Zeng, S. Qu, X. Han, Y. Deng, W. Hu, J. Lu, *Adv. Mater.* **2018**, *30*, 1703657; f) T. He, Y. Chen, Q. Liu, B. Lu, X. Song, H. Liu, M. Liu, Y.-N. Liu, Y. Zhang, X. Ouyang, S. Chen, *Angew. Chem. Int. Ed.* **2022**, *61*, e202201007; g) Y. Wang, T. Yang, X. Fan, Z. Bao, A. Tayal, H. Tan, M. Shi, Z. Liang, W. Zhang, H. Lin, R. Cao, Z. Huang, H. Zheng, *Angew. Chem. Int. Ed.* **2024**, *63*, e202313034.
[20] a) H. Dou, M. Xu, B. Wang, Z. Zhang, D. Luo, B. Shi, G. Wen, M. Mousavi, A. Yu, Z. Bai, Z. Jiang, Z. Chen, *Angew. Chem. Int. Ed.* **2021**, *60*, 5864–5870; b) H. Dou, M. Xu, B. Wang, Z. Zhang, G. Wen, F. Peng, K. Zarshenas, D. Luo, A. Yu, Z. Bai, Z. Jiang, Z. Chen, *Adv. Funct. Mater.* **2021**, *31*, 2104349.
[21] a) C. Chen, Y.-L. S. Tse, G. E. Lindberg, C. Knight, G. A. Voth, *J. Am. Chem. Soc.* **2016**, *138*, 991–1000; b) C.-X. Zhao, J.-N. Liu, N. Yao, X. Zeng, A. Chen, P. Dong, Y. Zhang, X. Ma, C. Tang, B.-Q. Li, Q. Zhang, *Renewables* **2023**, *1*, 73–80.
[22] a) M.-T. Lee, *J. Phys. Chem. C* **2019**, *123*, 10802–10815; b) L. Zou, Y.-S. Wei, C.-C. Hou, M. Wang, Y. Wang, H.-F. Wang, Z. Liu, Q. Xu, *CCS Chem.* **2022**, *4*, 194–204.
[23] a) D. Dong, X. Wei, J. B. Hooper, H. Pan, D. Bedrov, *Phys. Chem. Chem. Phys.* **2018**, *20*, 19350–19362; b) W. Chen, X. Wu, T. Li, X. Yan, Y. Zhang, X. Wang, F. Zhang, S. Zhang, G. He, *Chem. Eng. Sci.* **2021**, *244*, 116791; c) Z. Guo, Y. Yu, C. Li, E. Campos dos Santos, T. Wang, H. Li, J. Xu, C. Liu, H. Li, *Angew. Chem. Int. Ed.* **2024**, *63*, e202319913.
[24] S. Shinde, N. Wagh, C. Lee, D. Kim, S. Kim, H. Um, S. Lee, J. Lee, Scaling-Up Insights for Zinc-Air Battery Technologies Realizing Reversible Zinc Anodes[J]. *Adv. Mater.* **2023**, *35*, 2303509.

Manuscript received: April 18, 2024
Accepted manuscript online: June 18, 2024
Version of record online: July 29, 2024